JCI insight

$\alpha_v\beta_3$ Integrin drives fibroblast contraction and strain stiffening of soft provisional matrix during progressive fibrosis

Vincent F. Fiore, … , James S. Hagood, Thomas H. Barker

JCI Insight. 2018;3(20):e97597. https://doi.org/10.1172/jci.insight.97597.

Research Article | Cell biology | Pulmonology

Graphical abstract

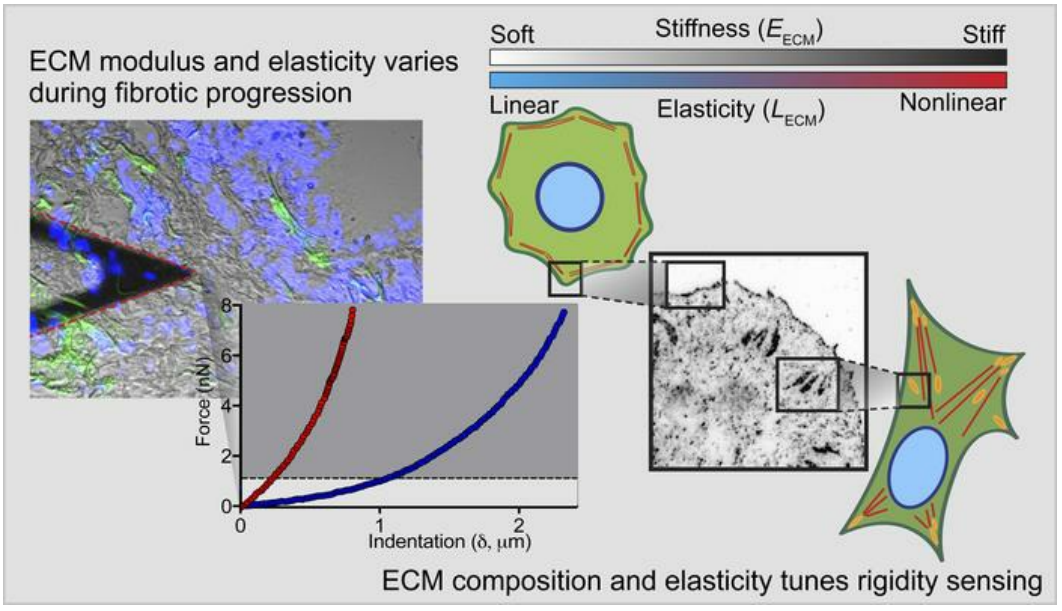

Find the latest version:

https://jci.me/97597/pdf

JCI insight

RESEARCH ARTICLE

$\alpha_v\beta_3$ Integrin drives fibroblast contraction and strain stiffening of soft provisional matrix during progressive fibrosis

Vincent F. Fiore,[1] Simon S. Wong,[2] Coleen Tran,[1] Chunting Tan,[2] Wenwei Xu,[3] Todd Sulchek,[3] Eric S. White,[4] James S. Hagood,[2,5] and Thomas H. Barker[6]

[1]Department of Biomedical Engineering, Georgia Institute of Technology, Atlanta, Georgia, USA. [2]Department of Pediatrics, Division of Pediatric Respiratory Medicine, University of California, San Diego, La Jolla, California, USA. [3]School of Mechanical Engineering, Georgia Institute of Technology, Atlanta, Georgia, USA. [4]Department of Internal Medicine, Division of Pulmonary and Critical Care Medicine, University of Michigan, Ann Arbor, Michigan, USA. [5]Rady Children's Hospital of San Diego, San Diego, California, USA. [6]Department of Biomedical Engineering, University of Virginia, Charlottesville, Virginia, USA.

Fibrosis is characterized by persistent deposition of extracellular matrix (ECM) by fibroblasts. Fibroblast mechanosensing of a stiffened ECM is hypothesized to drive the fibrotic program; however, the spatial distribution of ECM mechanics and their derangements in progressive fibrosis are poorly characterized. Importantly, fibrosis presents with significant histopathological heterogeneity at the microscale. Here, we report that fibroblastic foci (FF), the regions of active fibrogenesis in idiopathic pulmonary fibrosis (IPF), are surprisingly of similar modulus as normal lung parenchyma and are nonlinearly elastic. In vitro, provisional ECMs with mechanical properties similar to those of FF activate both normal and IPF patient–derived fibroblasts, whereas type I collagen ECMs with similar mechanical properties do not. This is mediated, in part, by $\alpha_v\beta_3$ integrin engagement and is augmented by loss of expression of Thy-1, which regulates $\alpha_v\beta_3$ integrin avidity for ECM. Thy-1 loss potentiates cell contractility-driven strain stiffening of provisional ECM in vitro and causes elevated $\alpha_v\beta_3$ integrin activation, increased fibrosis, and greater mortality following fibrotic lung injury in vivo. These data suggest a central role for $\alpha_v\beta_3$ integrin and provisional ECM in overriding mechanical cues that normally impose quiescent phenotypes, driving progressive fibrosis through physical stiffening of the fibrotic niche.

Introduction

Progressive fibrosis, resulting in disruption of organ function, is a major cause of morbidity and mortality worldwide. The aberrant and persistent activation of fibroblasts within a stiffened extracellular matrix (ECM) characterizes pathological fibrosis in multiple organs and in cancer (1–3). Our understanding of the transition from normal to diseased stroma is incomplete; however, it is increasingly clear that both intrinsic changes in cell phenotype and accumulation of aberrant extrinsic cues cooperate to drive pathological progression (4–6).

In idiopathic pulmonary fibrosis (IPF), a fatal and incurable form of progressive fibrosis, fibrosis-associated fibroblasts (FAFs) accumulate within regions of high synthetic and ECM remodeling activity, termed fibroblastic foci (FF) (7). Fibroblasts are sensitive to the mechanics of their microenvironment, which has led to the hypothesis that aberrant tissue mechanics drives fibrotic responses. Stiffer ECMs associated with mature fibrosis (MF) promote engagement of focal adhesions (FAs) and actomyosin-mediated cell contraction, promoting fibroblast-mediated assembly and remodeling of ECM (8–10). Thereby, mechanical signals can amplify positive feedback between the ECM and cytoskeletal systems to drive persistent profibrotic phenotypes (2, 10).

Fibroblasts from tissue isolates exhibit marked phenotypic heterogeneity (11, 12). This is exacerbated in IPF due to the spatial and temporal heterogeneity of remodeling, i.e., the intermixture of normal lung parenchyma (NL), FF, MF, and cystic "honeycomb" features within biopsied tissue segments (13). At the level of ECM, both composition and mechanics of the lung are drastically altered in IPF. Matricellular and

Conflict of interest: The authors have declared that no conflict of interest exists.

License: Copyright 2018, American Society for Clinical Investigation.

Submitted: September 19, 2017
Accepted: August 30, 2018
Published: October 18, 2018

Reference information:
JCI Insight. 2018;3(20):e97597.
https://doi.org/10.1172/jci.insight.97597.

provisional ECM proteins associated with tissue repair (e.g., periostin, latent TGF-β–binding protein 1, fibronectin [FN]) are markedly increased, whereas basement membrane components are diminished (14). Studies aimed at quantitatively measuring the mechanical properties of lung tissue ex vivo have primarily sampled over large segments of the tissue, without particular focus on the microscale spatial heterogeneity that exists. We and others have reported the Young's modulus (i.e., stiffness [*E*]) of normal and fibrotic lung tissue in the range of 0.5–5 kPa and 1–100 kPa, respectively (10, 14, 15). However, microscale variations of stiffness and how they relate to altered ECM composition and/or cellular phenotypes and functions have heretofore remained unexplored.

In this study, we address this critical gap by first coregistering atomic force microscopy (AFM) mapping of tissue elasticity with conventional immunohistochemical analysis of human fibrotic lung tissue, with the goal of mapping the microarchitecture of the heterogeneous fibrotic features of IPF. We explored the synergistic roles of ECM biochemistry and biophysics, specifically FN-rich provisional ECM and its nonlinearly elastic mechanical properties, in promoting a FAF phenotype, and we contrasted this with the suppressive activity of physiologically soft Col1 ECM. We identify $\alpha_v\beta_3$ integrin engagement of provisional ECM as a driver of cytoskeletal remodeling and mechanotransduction by FAFs, and we demonstrated that pathophysiologically relevant augmentation of $\alpha_v\beta_3$ integrin engagement through loss of Thy-1 surface expression leads to enhanced fibroblast activation, strain stiffening of provisional ECM, and progression of fibrosis in an in vivo model of lung fibrosis, which would otherwise resolve.

Results

FF are soft and nonlinearly elastic, while MF is stiff and linearly elastic. Despite the general understanding that tissue stiffening is concurrent with fibrotic progression in multiple organs, a microscale mechanical characterization of the key histopathological features of lung fibrosis (i.e., normal alveolar wall, FF, MF) has not been achieved, due to the small spatial scale and heterogeneous nature of IPF. To map the mechanical properties of these features, we applied standard histochemical staining concurrent with AFM nanoindentation force mapping and post hoc image coregistration (Figure 1, A–E, and Supplemental Figure 1; supplemental material available online with this article; https://doi.org/10.1172/jci.insight.97597DS1). In line with previous work in mice and humans, normal alveolar interstitium (NL) had an average *E* of 1.49 ± 1.59 kPa (mean ± SD; Figure 1, F and G). FF, characterized by weak eosinophilic staining compared with MF, the presence of cellular FN (FN-EDA), and, typically, α-SMA–expressing cells, had an *E* of 1.97 ± 2.31 kPa, whereas MF within the same tissue sections, characterized by prominent eosinophilic staining and dense fibrillar collagen, had an *E* of 8.97 ± 11.22 kPa (Figure 1, F and G). The regions of most active fibrogenesis, the FF, are therefore relatively soft and are quantitatively more similar to NL than regions of MF. Additionally, modest spatial gradients in modulus were observed, particularly in FF (Figure 1D). Because FF are thought to occur earlier than MF in fibrotic progression, these data challenge the hypothesis that normal, physiological fibroblast rigidity sensing of a stiff microenvironment is an initial driver of fibrotic development.

During our measurements of tissue modulus, we observed substantial strain stiffening of the resultant modulus measured; this was especially prominent in NL and FF. This effect is well known for biopolymer networks and is due to the nonlinear force-displacement relationship of individual network fibers and changes in fiber alignment between bending and stretching modes (16). To quantify the effect of nonlinear elasticity, we used a point-wise Young's modulus to measure *E* as a function of indentation depth (i.e., loading; Figure 1B). This yielded a low strain regime of relative linear elasticity (E_{low}) and high strain regime (E_{high}) where modulus monotonically increased. These values consistently corresponded to 10%–30% of the loading curve and 70%–90% (~6 nN max load; Figure 1B), respectively. To obtain a readily comparable parameter describing nonlinear elasticity, we measured *E* values of these two regimes and calculated an elasticity metric, $L = E_{low}/E_{high}$, where $L = 1$ is absolute linear elasticity and values less than 1 are increasingly nonlinear.

We found that both NL and FF were highly nonlinear ($L \approx 0.6$), whereas MF, which are also the regions of highest stiffness, were nearly linearly elastic ($L = 0.85 \pm 0.34$; Figure 1, E, G, and H). Microscale features of high modulus showed a modest correlation with greater linear elasticity (Supplemental Figure 2). Thus, fibrotic tissue maturation is associated with both an increase in tissue modulus and a transition from nonlinear to linear elasticity; whereas normal alveolar walls and FF are soft and nonlinearly elastic, MF is stiff and more linearly elastic.

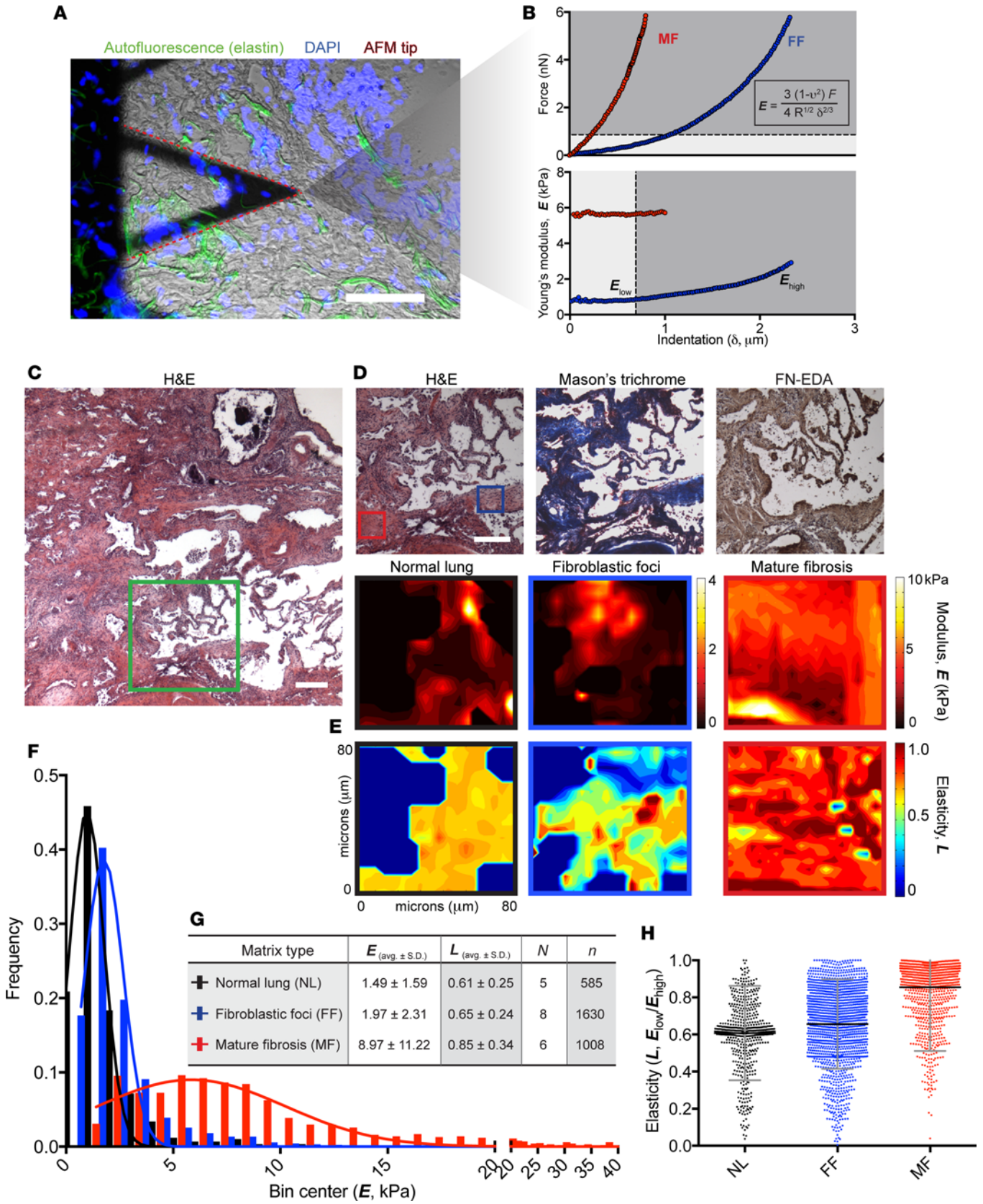

Matrix type	E (avg. ± S.D.)	L (avg. ± S.D.)	N	n
Normal lung (NL)	1.49 ± 1.59	0.61 ± 0.25	5	585
Fibroblastic foci (FF)	1.97 ± 2.31	0.65 ± 0.24	8	1630
Mature fibrosis (MF)	8.97 ± 11.22	0.85 ± 0.34	6	1008

Figure 1. Characterization of microscale IPF tissue rigidity and elasticity. (**A**) Experimental setup of atomic force microscope (AFM) mechanical measurements, depicting the cantilever (red dotted line) overlying lung tissue. Fluorescence images were acquired using an inverted optical microscope in combination with AFM. DAPI (cell nuclei), tissue autofluorescence (mainly elastin microfibrils), and phase-contrast images are shown. Scale bar: 100 μm. (**B**) Example force indentation and Young's modulus (*E*) indentation curves of fibroblastic foci (FF, blue) and mature fibrosis (MF, red) regions; the low indentation

regime, E_{low}, is highlighted (pink dotted line, gray background) and the linearly elastic regime indentation limit, δ_L, is demarked (black dotted line, bottom). The equation to calculate Young's modulus from force indentation is shown. (**C**) H&E staining of IPF tissue. Scale bar: 200 μm. (**D**) Magnified views of the region in **C** (green; zoom in region) stained for H&E, Masson's trichrome, and fibronectin-EDA (FN-EDA, with regions of interest, including FF (blue box) and MF (red box), indicated. Scale bar: 100 μm. (**E**) AFM force maps with *E* ("black-red-white" heatmap, range 0–4 kPa for NL and FF; 0–10 kPa for MF) and elasticity (*L*; "rainbow" heatmap) shown for NL (data not shown), FF (blue box), and MF (red box), with regions of interest depicted in **D**. (**F**) Histogram of *E* values are shown for normal lung (NL, black; $n = 5$), FF (blue; $n = 8$), and MF (red; $n = 6$) regions from 2 patients, and Gaussian functions were fit to the distributions. (**G**) *E* and *L* values for the number of regions (*N*) and measurements (*n*). (**H**) Dot plots and the mean ± SD of *L* for the complete data set is shown.

Soft, FN-rich provisional ECM is sufficient to drive activation of normal and FAFs in vitro. To dissect potential effects of the observed tissue mechanics on fibroblast activation, we used defined in vitro culture substrates to approximate the mechanics and ECM compositions observed in vivo. In the case of nonlinearly elastic, type I collagen-rich ECM present in NL interstitium, we used polymerized collagen I gels (Col1 gel, 3.3 mg/ml), which have been previously shown to repress normal fibroblast activation (17, 18), and we characterized these Col1 gels to have a modulus ($E = 0.43 \pm 0.22$ kPa) and elasticity ($L = 0.54 \pm 0.13$) comparable to that of NL (Figure 2, A and B). Both normal and IPF fibroblasts cultured on this model substrate exhibited a stellate morphology, with a lack of prominent actin stress fibers or large FAs (Figure 2C). Consistently, measuring the spread area of individual cells, a measure of cytoskeletal remodeling and activity, showed that both IPF and NL fibroblasts (NLFs) show diminished spreading on Col1 gels compared with active and proliferative fibroblasts on stiff high-density fibrillar Col1 (high-density fibrillar collagen [HDFC]; $E = 21.96 \pm 8.82$ kPa) or FN-adsorbed glass (FN-gl; Figure 2D). As a consequence of cytoskeletal remodeling in response to ECM stiffness, polymerization of actin filaments enables nuclear translocation of the transcriptional coactivator MRTF-A, where, together with serum response factor, it activates a profibrotic gene expression program, including *Acta2* (α-SMA) and *Col1a1*/*Col1a2* (Col1 subunits) (19, 20). We found strong suppression of MRTF nuclear translocation in both normal and IPF lung fibroblasts on soft ColI gels, in particular compared with HDFC and FN-gl, which both strongly drove MRTF-A into the nucleus (Figure 2E).

To mimic the provisional ECM character of FF, we used fibroblast cell–derived matrices (CDMs). Importantly, NIH-3T3 fibroblasts assembled a FN-rich provisional matrix that exhibited low stiffness ($E = 0.63 \pm 0.29$ kPa) and was highly nonlinearly elastic ($L = 0.60 \pm 0.12$), similar to the features identified for FF tissue (Figure 2, C and D). Both IPF and normal fibroblasts cultured on CDMs exhibit marked cytoskeletal remodeling, as shown by increased cell spreading, stress fiber formation, and enhanced FA assembly, despite the very soft nature of this provisional ECM, consistent with prior studies (Figure 2C) (21). On CDMs, fibroblast MRTF-A nuclear localization was enhanced, indicating an increase in fibroblast activation compared with normal and IPF fibroblasts on Col1 gels where MRTF-A was localized to the cytoplasm (Figure 2, C–E). Interestingly, MRTF-A nuclear localization on CDMs was observed in both normal and IPF fibroblasts, albeit to a slightly greater extent in IPF fibroblasts, suggesting additional intrinsic differences in fibroblast populations may also play a role. To mimic the substrate of MF, we used HDFCs, which supported maximal cell spreading and MRTF-A nuclear translocation to levels seen on FN-gl or Col1-gl (Figure 2, C–E, and Supplemental Figure 2). These data support the hypothesis that both ECM mechanics and their biochemical constituency (e.g., FN versus Col1) strongly influence fibroblast activation and indicate that provisional ECMs activate fibroblasts even when extremely soft. However, it should be noted that soft polyacrylamide (PA) gels, which display linearly elastic behavior, presenting covalently coupled solubilized CDM were not sufficient to activate fibroblasts perhaps, suggesting that the fibrillar architecture and/or the nonlinear elastic behavior of CDM is a necessary feature (Supplemental Figure 3, A–D).

$\alpha_v\beta_3$ Integrin engagement of soft provisional ECM enhances fibroblast activation. A critical difference between the FN-rich provisional ECMs and the Col1-rich mature ECMs prominent in varying stages of pathologic fibrosis is the subset of integrins they engage. While β_1 integrins engage both collagen- and FN-rich ECMs, α_v heterodimers primarily engage ECM proteins containing the RGD tripeptide motif or variations thereof. We previously discovered that elevated α_v integrin ligation of FN matrices is responsible for aberrant rigidity sensing in FAFs due to loss of Thy-1 (also known as CD90) cell surface expression (22). Here, on CDMs, normal fibroblasts exhibited $\alpha_v\beta_3$ enrichment in FAs, where they colocalized with active β_1 integrin, paxillin, and active FAK (FAK-pY397; Figure 3, A and B, and Supplemental Figure 4A); similarly, $\alpha_v\beta_3$ was enriched in FAs on FN-gl (Figure 3, A and B). In contrast, $\alpha_v\beta_3$ was absent from FAs on Col1 gels (Figure 3, A and D) and, intriguingly, also on soft, linearly elastic CDM-PA (Supplemental Figure 3, E and F), which, in theory, is capable of ligating $\alpha_v\beta_3$ integrin. Antibody blockade of $\alpha_v\beta_3$ on CDMs caused a substantial shift

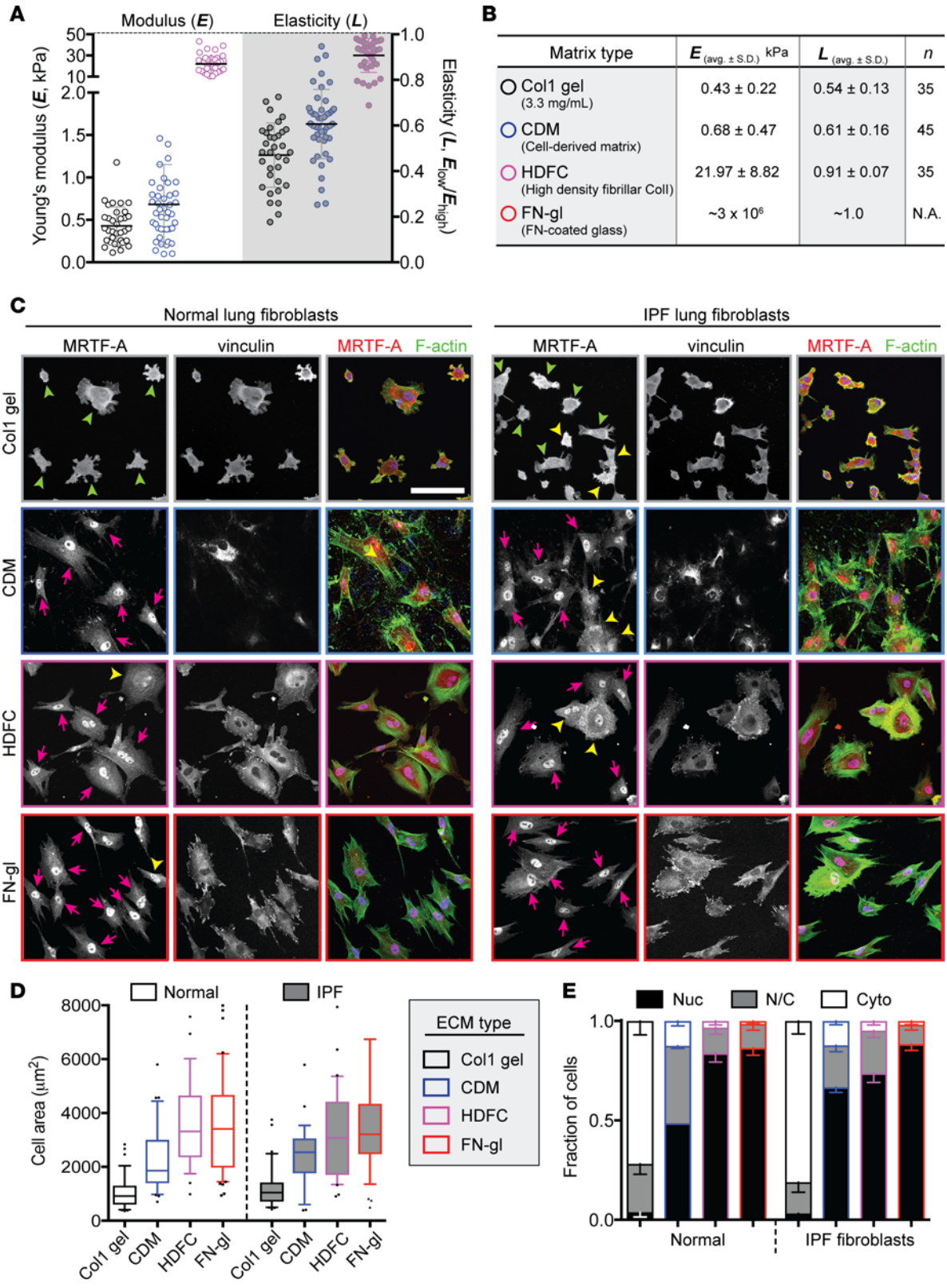

Matrix type	$E_{(avg. \pm S.D.)}$ kPa	$L_{(avg. \pm S.D.)}$	*n*
Col1 gel (3.3 mg/mL)	0.43 ± 0.22	0.54 ± 0.13	35
CDM (Cell-derived matrix)	0.68 ± 0.47	0.61 ± 0.16	45
HDFC (High density fibrillar Col1)	21.97 ± 8.82	0.91 ± 0.07	35
FN-gl (FN-coated glass)	~3 x 10^6	~1.0	N.A.

Figure 2. Fibroblast activation is modulated by extracellular matrix type, modulus, and elasticity. (**A**) Extracellular matrix (ECM) Young's modulus (*E*) and elasticity (*L*) of type I collagen (Col1) gels, cell-derived matrices (CDMs), or high-density fibrillar collagen (HDFC) matrices, as measured by AFM. Individual data points and mean ± SD are shown. (**B**) *E* and *L* values (mean ± SD) for the number of measurements (*n*). Approximate values of *E* and *L* for FN-gl are listed. (**C**) Immunofluorescence images of normal or IPF lung fibroblasts cultured on the indicated substrates stained for MRTF-A (gray; red, overlay), vinculin (gray), F-actin (green, overlay), and DAPI (blue, overlay). Nuclear (pink arrows), nuclear and cytoplasmic (yellow arrowheads), and cytoplasmic (green arrowheads) MRTF-A staining is denoted. (**D**) Box-and-whisker plots (10th–90th percentiles, with outliers) of cell

area from 2 independent experiments of normal and IPF lung fibroblasts cultured on Col1 gels (black outline), CDMs (blue outline), HDFC (magenta outline), or FN-gl (red outline) substrates. (**E**) Fraction of cells with nuclear (Nuc, black fill), nuclear and cytoplasmic (N/C, gray fill), and cytoplasmic (Cyto, white fill) MRTF-A localization (mean ± SEM) in the same conditions as in **D**. Scale bar: 100 μm.

of MRTF-A localization out of the nucleus and into the cytoplasm, concurrent with a decrease in F-actin stress fibers, supporting a reduction in CDM-dependent fibroblast activation (Figure 3, C and D). Thus, $\alpha_v\beta_3$ integrin ligation of provisional ECM supports fibroblast activation, despite its low modulus, and the loss of this ligation diminishes fibroblast activation.

Disinhibition of $\alpha_v\beta_3$ integrin avidity and signaling, via Thy-1 knockdown, augments fibroblast activation in soft provisional ECM. We recently found that Thy-1 behaves as a *cis*-acting adapter of α_v integrins, where it acts to restrain α_v-FN binding, activation, and signaling on soft substrates (22). Here, we used modulation of Thy-1 expression to enhance basal α_v integrin avidity for ECM, either in endogenous fibroblast subpopulations or, more directly, through shRNA knockdown of Thy-1 in normal fibroblasts (Thy-1.shRNA; ~90% knockdown efficiency). While normal (cont.shRNA) fibroblasts did localize $\alpha_v\beta_3$ to FAs within soft CDMs, this was significantly enhanced upon Thy-1 knockdown, reaching levels similar to those observed on FN-gl, regardless of Thy-1 expression level (Figure 4, A and B). While MRTF-A was primarily localized to the nucleus in both Thy-1.shRNA and cont.shRNA cells on both CDMs and FN-gl (Figure 4, C and D), we noticed that Thy-1 knockdown elevated cortical stiffness on CDMs compared with cont.shRNA cells, indicating higher cell contractility (Figure 4, E and F). Thy-1.shRNA cells also had larger FAs and higher levels of FAK signaling on CDMs, reminiscent of the effect of Thy-1 loss on heightening $\alpha_v\beta_3$ avidity and cytoskeletal engagement during mechanotransduction of soft linearly elastic substrates (22). Cortical stiffness, FA size, and levels of active FAK signaling were all strongly and positively correlated with $\alpha_v\beta_3$ integrin enrichment in FAs, regardless of whether the enrichment was induced by ECM substrate or Thy-1.shRNA (Figure 4G and Supplemental Figure 4, A and B). These observations were consistent with endogenous subpopulations FACS-sorted for Thy-1 expression (Supplemental Figure 4, C–E). Collectively, these data strongly suggest a link between the capacity for $\alpha_v\beta_3$ integrin engagement of ECM and (a) FA assembly and maturation in soft ECMs and (b) intrinsically elevated cytoskeletal contractility mediated by disinhibition of α_v integrins in FAFs.

Disinhibition of $\alpha_v\beta_3$ integrin enables fibroblasts to strain-stiffen soft, nonlinearly elastic provisional ECMs. Applied forces can deform and locally stiffen nonlinearly elastic substrates by strain stiffening. In the context of lung tissue transitioning to scar, contractile myofibroblasts are likely sources of applied forces, and, based on our data from human IPF tissue, FF nonlinear elasticity may enable these cells to stiffen their microenvironment. To probe the local consequences of cell-mediated contractility of nonlinearly elastic CDMs, we measured ECM *E* proximal (<10 μm from cell boundary) or distal to cells in which integrin$_v\beta_3$ engagement is disinhibited. Regions close to cont.shRNA cells were approximately 0.5-fold stiffer than distal regions (Figure 5), indicating the ability of resident fibroblasts to strain stiffen provisional ECMs. However, cell-mediated strain stiffening was enhanced 2-fold (proximal to distal) in Thy-1.shRNA cells. This also coincided with increased elasticity, *L*, resulting in a shift from strain stiffening to more linearly elastic ECM (Figure 5).

To interrogate the function of $\alpha_v\beta_3$ specifically in the enhanced ECM strain stiffening due to Thy-1 loss, we blocked $\alpha_v\beta_3$ with function blocking antibody. This caused a significant reduction in not only the proximal *E*, but also the distal *E* and potently diminished ECM *L*, indicating that disinhibition of $\alpha_v\beta_3$ integrin further enhances the strain stiffening activity of fibroblasts, remodeling provisional ECMs toward a more MF-like mechanical character (i.e., nonlinearly elastic). In the context of a densely populated provisional ECM, such as those believed to constitute FF, ECM stiffening by resident fibroblasts is likely to be an important consequence of provisional matrix/integrin$_v\beta_3$-dependent cytoskeletal remodeling and contractility, which we now show is further augmented by intrinsic cell alterations occurring in the fibrotic niche (i.e., disinhibition of $\alpha_v\beta_3$ integrin via loss of Thy-1 surface expression), the underlying ECM ligand composition (i.e., FN's ability to engage $\alpha_v\beta_3$ integrin), and ECM mechanics — importantly, both the stiffness and elasticity.

$\alpha_v\beta_3$ Integrin activity correlates in vivo with the degree, duration, and mortality of lung fibrosis. To examine a potential role for the $\alpha_v\beta_3$ integrin during fibrogenesis in vivo, we induced fibrosis via intratracheal delivery of the chemotherapeutic agent bleomycin, a standard but self-resolving model of lung fibrosis. WT mice display a temporal increase in active $\alpha_v\beta_3$ integrin staining following bleomycin treatment, as denoted by immunostaining for the active conformation of $\alpha_v\beta_3$ (23). Levels of active $\alpha_v\beta_3$ peaked at 14 days and began to resolve at 28

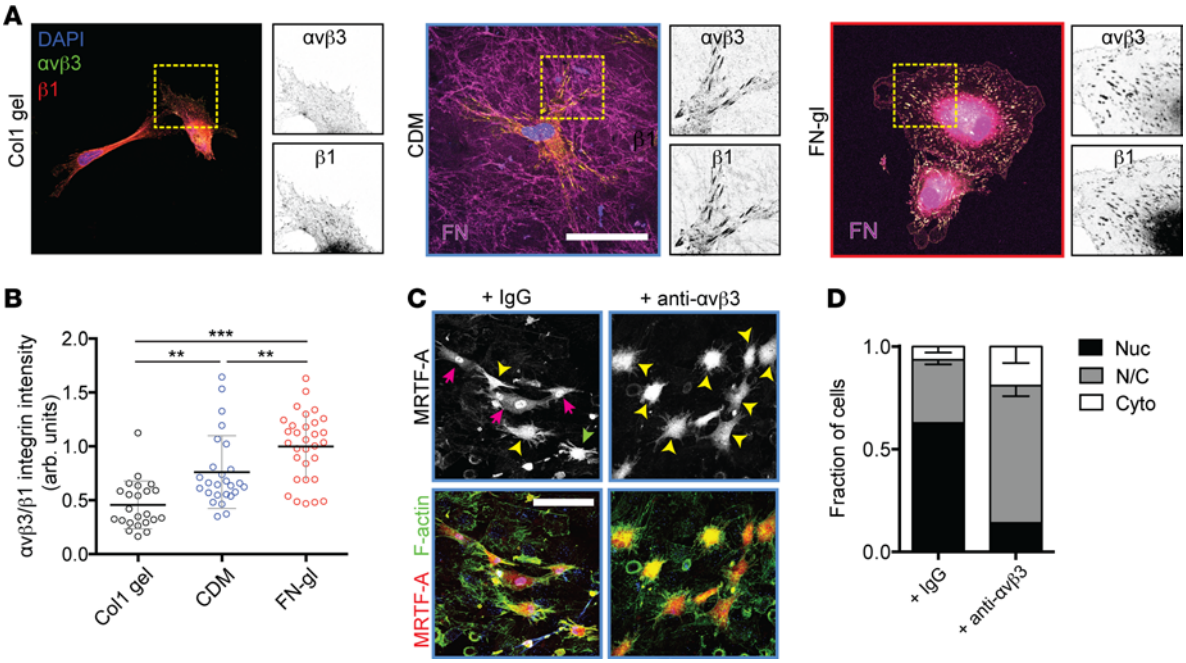

Figure 3. $\alpha_v\beta_3$ Integrin engagement of soft provisional ECM enhances fibroblast activation. (**A**) Immunofluorescence images of normal lung fibroblasts cultured on the indicated substrates stained for $\alpha_v\beta_3$ (green, overlay; gray), β_1 integrin (red, overlay; gray), and DAPI (blue, overlay). Zoomed regions (yellow box) are shown (inverted). FN staining (purple) is shown for CDM and FN-gl. Original magnification, ×60. (**B**) Integrin engagement was quantified for $\alpha_v\beta_3$ and β_1 integrins within segmented FAs by ratiometric pixel intensity. All identified FAs were averaged for a single cell; mean ± SD is shown for a minimum of $n = 15$ cells per group from 2 independent experiments. (**C**) Immunofluorescence images of normal lung fibroblasts on CDMs treated with anti-$\alpha_v\beta_3$ integrin antibody or IgG control stained for MRTF-A (gray; red, overlay), F-actin (green, overlay), and DAPI (blue, overlay). Nuclear (pink arrows), nuclear and cytoplasmic (yellow arrowheads), and cytoplasmic (green arrowheads) MRTF-A staining is denoted. (**D**) The fraction of cells with nuclear (Nuc, black fill), nuclear and cytoplasmic (N/C, gray fill), and cytoplasmic (Cyto, white fill) MRTF-A localization (mean ± SEM) in conditions the same conditions as in **C**. One-way ANOVA and Newman-Keuls multiple comparisons post hoc test was used to calculate statistical significance. $^{**}P < 0.01$; $^{***}P < 0.001$ between indicated groups. Scale bar: 100 μm.

days with a near-complete return to baseline levels by day 42 (Figure 6, A and B). This time course was strongly correlated with fibrotic development and resolution (Figure 6C). Particularly, we found that levels of active $\alpha_v\beta_3$ follow a similar trend as pulmonary elastic resistance over the course of the study (Supplemental Figure 5). This phenotype is in stark contrast to Thy-1$^{-/-}$ mice; we observed elevated $\alpha_v\beta_3$ activity at baseline in untreated lungs, albeit not sufficient to spontaneously induce fibrosis. Upon instillation of bleomycin, we observed a similar increase in $\alpha_v\beta_3$ activity at day 14, but, in contrast to that in WT lungs, the activity was sustained at all subsequent time points through day 56 (Figure 6, A and B). Similar to that in WT mice, Thy-1$^{-/-}$ mice exhibited a strong correlation between $\alpha_v\beta_3$ activity and pulmonary elastic resistance (Figure 6D). Concomitantly with increased whole lung stiffness, we observed severe and sustained alveolar destruction, septal thickening, and fibrotic appearance (i.e., extensive connective tissue deposition) in histopathological sections through day 56 in Thy-1$^{-/-}$ mice, whereas WT lungs returned to relatively normal appearance by day 42 (Figure 6C). The persistent, nonresolving fibrosis and corresponding elevation in $\alpha_v\beta_3$ integrin activation correlated with decreased survival after bleomycin challenge (Figure 6E), a normally nonfatal model.

Discussion

A major theory in fibrosis posits that the mechanical microenvironment, specifically stiffening of the ECM, drives transformation of stromal cells to scar-forming myofibroblasts, which further exacerbates fibrotic remodeling (2, 10, 20, 24). Yet significant gaps in this theory remain unanswered. We have found that the mechanical properties of FF are surprisingly similar to those of NL interstitium. In particular, these regions have a low E compared with MF and exhibit nonlinear elasticity or strain stiffening. The softness of FF is perhaps surprising, given the close association between FF burden and clinical outcomes, much of the morbidity of which is related to decreased lung compliance or increased organ stiffness (25–28). Furthermore, numerous in vitro studies have demonstrated a profibrotic role for MF-like substrate E and an antifibrotic role for NL- and FF-like E (4, 10, 15, 20, 22). Thus, an apparent discrepancy arises for the

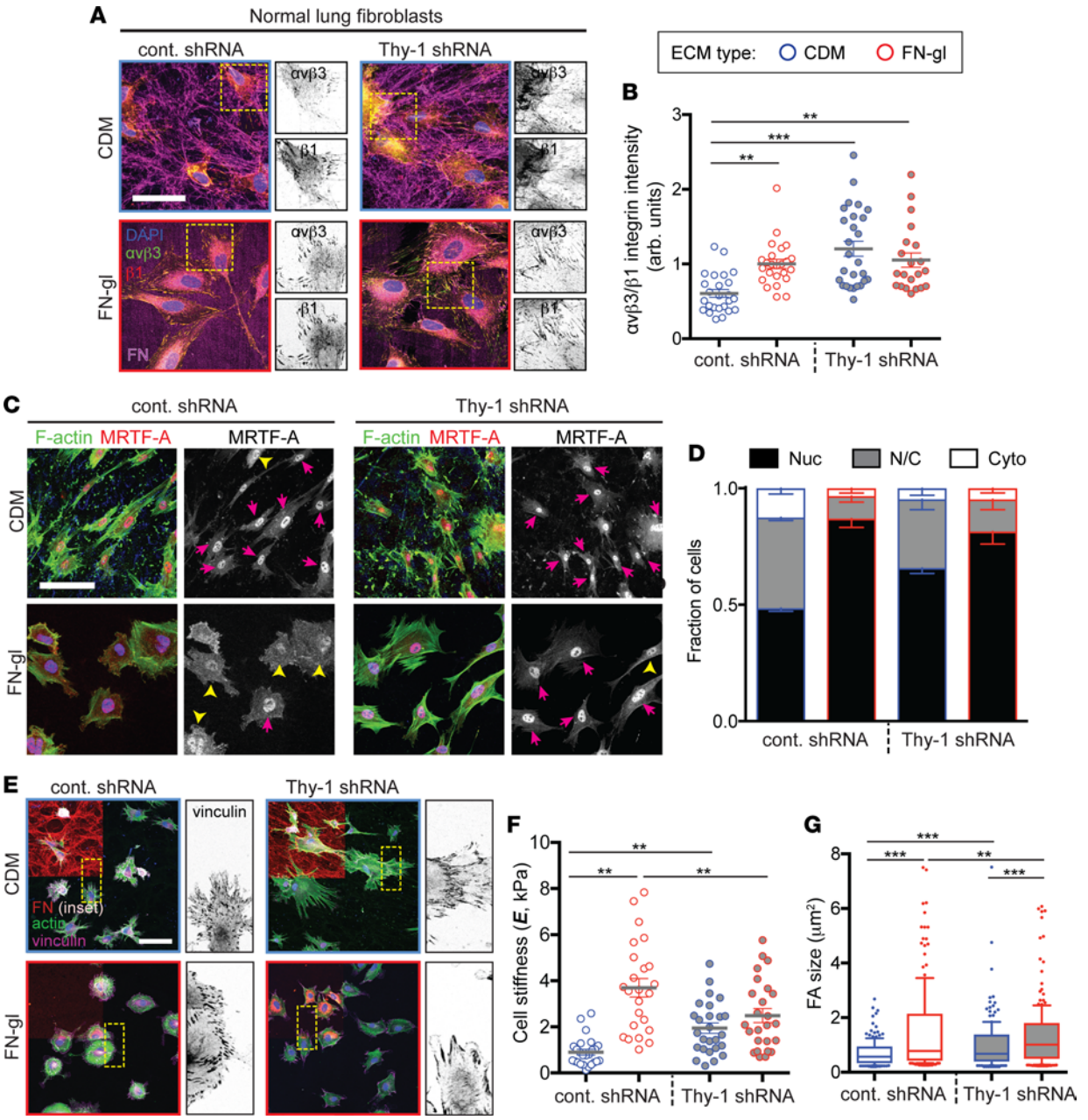

Figure 4. Disinhibition of $\alpha_v\beta_3$ integrin enables fibroblasts to strain-stiffen soft, nonlinearly elastic provisional ECMs. (**A**) Immunofluorescence images of NLFs transduced cont.shRNA or Thy-1.shRNA NLFs cultured on CDMs and FN-gl; FN (purple, overlay), $\alpha_v\beta_3$ (green, overlay; gray), and β_1 integrin (red, overlay; gray) are shown. (**B**) Quantification of $\alpha_v\beta_3$ versus β_1 integrin engagement. All identified FAs were averaged for a single cell; data are shown for a minimum of n = 15 cells from 2 independent experiments. (**C**) Immunofluorescence images of cont.shRNA and Thy-1.shRNA fibroblasts cultured on CDMs and FN-gl stained for MRTF-A (red, overlay; gray, right) and F-actin (green, overlay), representative of 2 independent experiments. Nuclear (pink arrows), nuclear/cytoplasmic (yellow arrowheads), and cytoplasmic (yellow arrowheads) MRTF-A staining is denoted. (**D**) Fraction of cells with nuclear (Nuc, black fill), nuclear and cytoplasmic (N/C, gray fill), and cytoplasmic (Cyto, white fill) MRTF-A localization (mean ± SEM) in the same conditions as in **C**. (**E**) Cont.shRNA or Thy-1.shRNA fibroblasts cultured on CDMs or FN-gl; F-actin (green), vinculin (purple), and nuclei (blue) are overlaid for the entire viewing field; FN (red) is overlaid for the corresponding area (inset, top left); and a magnified view (yellow box) of vinculin is shown (inverted, right). (**F**) Single-cell stiffness measurements for cont.shRNA and Thy-1.shRNA fibroblasts, labeled as in **C**. Data shown are pooled from 3 independent experiments. (**G**) Box-and-whisker plots of FA area for a minimum of n = 10 cells from 2 independent experiments are shown. One-way ANOVA and Newman-Keuls multiple comparisons tests were used to calculate statistical significance. $^{**}P < 0.01$; $^{***}P < 0.001$ between indicated groups. Scale bar: 100 μm. Error bars are SEM.

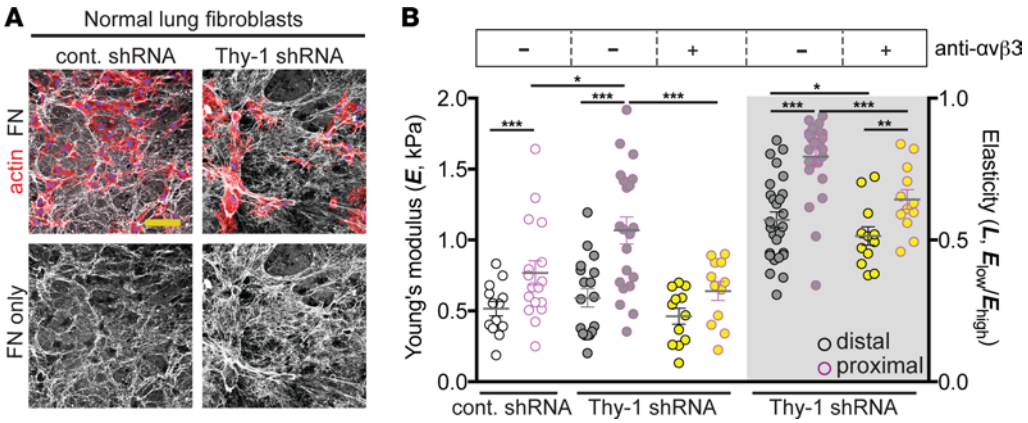

Figure 5. $\alpha_v\beta_3$ Integrin engagement potentiates fibroblasts contractility and strain stiffening of soft, nonlinearly elastic provisional ECM. (**A**) Immunofluorescence images of cont.shRNA or Thy-1.shRNA fibroblasts cultured on CDMs; actin (red), FN matrix (gray), or FN matrix only (gray) are shown. (**B**) AFM stiffness measurements of the ECM were taken either within 10 μm (proximal, purple outline) or greater than 10 μm (distal, black outline) from the cell body. ECM Young's modulus (*E*) and elasticity (*L*) of distal versus proximal measurements for each shRNA treatment and Thy-1. shRNA fibroblasts treated with anti-$_{v3}$ blocking antibody are shown. Dot plots and the mean ± SEM are shown, and statistical significance was calculated using a Kruskal-Wallis nonparametric test with Dunn's multiple comparison. **P* < 0.05; ***P* < 0.01; ****P* < 0.001 between indicated groups. Scale bar: 100 μm.

role of substrate *E* in determining fibroblast phenotype. We hypothesize that this is because in vitro studies typically vary the magnitude of substrate *E* using linearly elastic substrates (i.e., PA gels) with covalently bound soluble forms of ECM proteins, which likely does not recapitulate integrin ligation, activation, and mechanotransduction within endogenous tissue microenvironments.

While the nonlinear elasticity of lung has long been known from measurements at the whole-organ and macroscopic (millimeter) tissue scales (29–32), this is, to our knowledge, the first work to our knowledge demonstrating the prominence of this phenomenon at the local (microscale) level at which cells sense mechanical cues. What are the potential effects of local ECM nonlinear elasticity on IPF progression? Cells within a nonlinearly elastic matrix can locally strain stiffen their microenvironment, which may be occupied by neighboring cells that increase their own contractility in response. In this way, positive feedback between cell contractility and ECM remodeling may elicit spatially correlated and cooperative tissue stiffening. Intriguingly, there appears to be a reciprocal role for the cell mechanotransduction phenotype in eliciting changes to local ECM mechanics. Coordination among distinct integrin heterodimers, namely $\alpha_v\beta_3$ and $\alpha_5\beta_1$, are necessary for fibroblast rigidity sensing of linearly elastic FN substrates (33–35). $\alpha_v\beta_3$-FN bonds have been shown to be weaker, but occur faster, than $\alpha_5\beta_1$-FN bonds and undergo force-mediated strengthening and recruit other integrin heterodimers to the FA. These coordinated events dynamically couple actomyosin forces and receptor-ligand dynamics (36–38) and lead to the application of cell-derived forces on ECM structures. We have shown that, upon Thy-1 loss, $\alpha_v\beta_3$ avidity to FN substrates is disinhibited, which enables $\alpha_v\beta_3$ engagement, FA signaling, and the activation of actomyosin machinery to enhance cell contractility on soft, linearly elastic substrates (22). Here, we show that enhancing $\alpha_v\beta_3$ engagement (via provisional ECM and disinhibition via Thy-1 knockdown) stimulates fibroblast contractility and, consequently, stiffening of soft, nonlinearly elastic ECM. This suggests that fibroblast subpopulations with $\alpha_v\beta_3$ integrin dysregulation may amplify mechanical conditioning of the ECM by increasing fibroblast contractility. This tendency to strain stiffen provisional ECM may have the effect of activating neighboring interstitial cells, thus effecting the spread of fibrosis. Perhaps not surprisingly, α_v integrins, more broadly, have demonstrated potent roles in fibrosis of many tissue types, perhaps most notably in the mechanoactivation of TGF-β (39). Interestingly, Thy-1 loss is also associated with acute lung injury (40) and aging (41), and it is linked to fibrosis-associated phenotypes (42–47), including enhanced activation of TGF-β (48, 49). While it is not entirely clear how or why Thy-1–negative FAFs emerge in the early fibrotic milieu, our previous work has shown that Thy-1 is transiently lost in response to inflammatory cytokine signaling (50) and epigenetically silenced within FF of IPF (51). Once present within FF, FAFs may contribute to both the composition and mechanical properties of the ECM microenvironment. Thus, although injury-associated provisional ECM can activate resident fibroblasts, we suggest that the triad of FN, nonlinear elasticity,

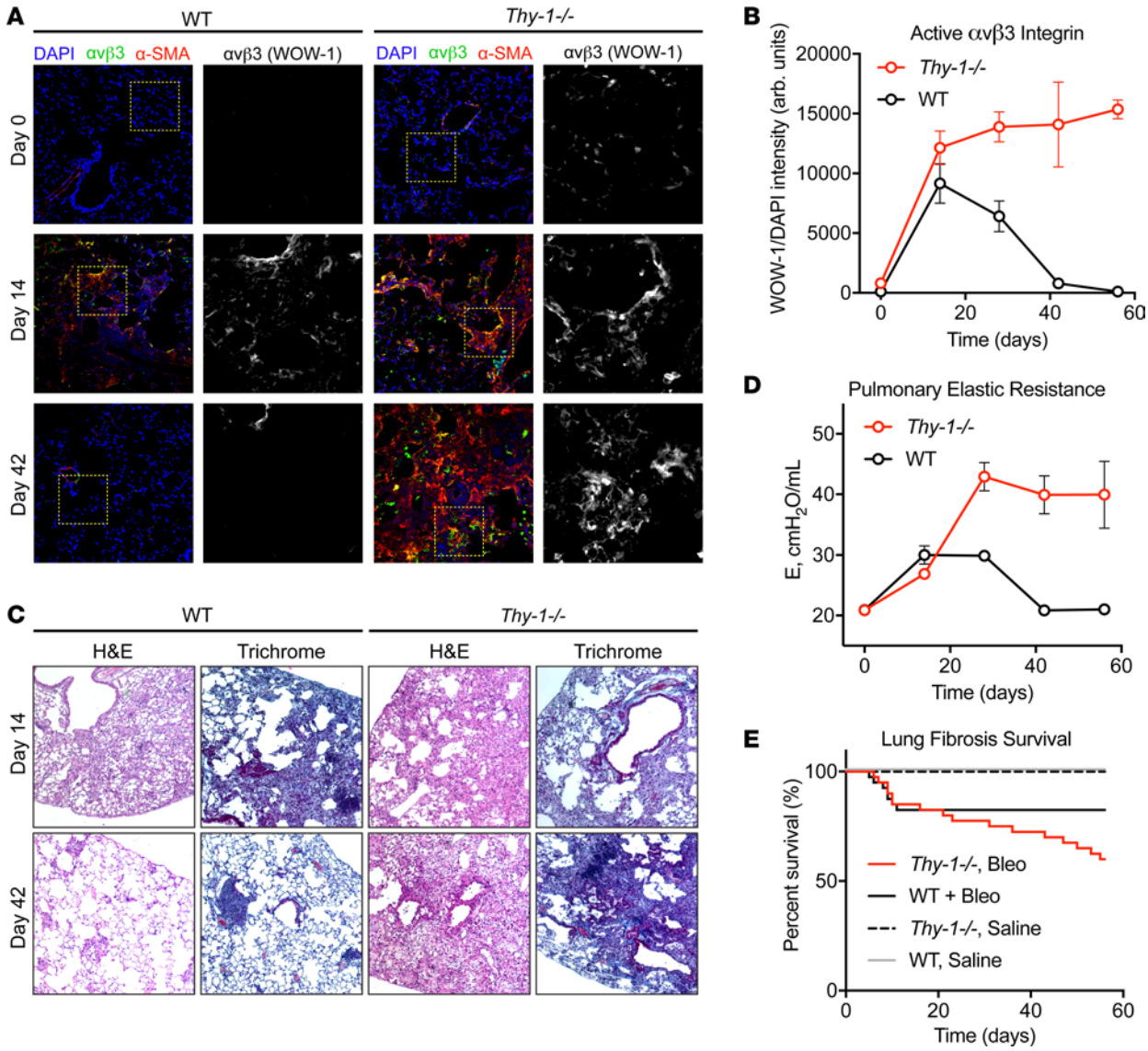

Figure 6. *Thy-1* loss elevates $\alpha_v\beta_3$ integrin activity and causes progressive fibrosis in a model of lung fibrosis. (**A**) Immunofluorescence images of active $\alpha_v\beta_3$ (WOW-1 Ab, green), α-SMA (red), and nuclei (blue) in lung tissue sections in WT and *Thy-1*$^{-/-}$ mice at 0, 14, and 42 days after intratracheal bleomycin treatment to induce fibrosis. A magnified image (yellow box) of active $\alpha_v\beta_3$ is shown (gray, right). Original magnification, ×20. (**B**) Quantification of WOW-1 staining intensity in WT (black outline) and *Thy-1*$^{-/-}$ (red outline) lungs at 14, 28, 42, and 56 days following bleomycin treatment. (**C**) H&E and Mason's trichrome staining of WT and *Thy-1*$^{-/-}$ mice 14 and 42 days after bleomycin treatment. Note sustained alveolar destruction and connective tissue deposition in *Thy-1*$^{-/-}$ lungs 42 days after bleomycin, while WT lungs are largely normal. Original magnification, ×10. (**D**) Quantification of pulmonary elastic resistance from whole-lung forced oscillation maneuvers in WT and *Thy-1*$^{-/-}$ mice over time after bleomycin treatment. (**E**) Kaplan-Meyer survival curve for WT and *Thy-1*$^{-/-}$ mice after bleomycin treatment. Error bars are SEM.

and elevated $\alpha_v\beta_3$ integrin activation in "primed" FAF subpopulations, due to loss of Thy-1, may promote progression of lesions through enhanced strain stiffening and recruitment of neighboring fibroblasts into the stiffness-driven fibrotic program.

Methods

Human tissue procurement. Human lungs deemed to be unsuitable for lung transplantation were obtained from beating-heart (or warm autopsy) donors through Gift of Life Michigan. Human deidentified IPF lung samples were obtained from explants of patients with IPF undergoing lung transplantation at the University of Michigan. Excised tissue cores were submerged in a 3:1 30% sucrose/OCT mixture and maintained at –20 mmHg for 1 hour. They were then embedded in OCT and flash frozen in a dry ice/isopentane bath or immediately flash frozen in liquid nitrogen; samples were stored at –80°C. Serial cryosections were

obtained, and samples for AFM were immediately brought to room temperature in PBS with protease inhibitors (cOmplete Mini, Roche), labeled with Hoechst 33258 (Invitrogen), and prepared with gridded coverglass for downstream image coregistration.

AFM mechanical measurements. An MFP-3D AFM (Asylum Research) with a TiU-inverted optical microscope (Nikon) was used for all AFM experiments. AFM nanoindentation tests were performed in medium using a 4.74-μm diameter spherical tipped silicon nitride cantilever (Bruker). Cantilever spring constants were measured prior to sample analysis using the thermal fluctuation method, with nominal values of 30–50 pN/nm. For lung tissue measurements, samples were maintained in PBS with protease inhibitors. Bright-field, nuclei (Hoechst), and elastin/collagen autofluorescence images were captured using standard DAPI/FITC/TRITC filter cubes (Nikon) and used to align the cantilever to the sample and for image coregistration. Two-dimensional force maps were taken in 20 × 20 μm, 40 × 40 μm, or 80 × 80 μm square grids, with between 8 and 20 sample points per axial dimension. AFM measurements were made using a cantilever deflection set point of approximately 6 nN and an indentation rate of 22 μm/s. In all experiments, the deflection of the cantilever did not exceed the linearity of the photodiode detector, even for forces up to 10 μN. Force-indentation curves were analyzed using a modified Hertz model for contact mechanics of spherical elastic bodies. The sample Poisson's ratio was assumed as 0.4 (52), and a power law of 1.5 was used to model tip geometry, as previously described (15). To obtain the pointwise Young's modulus, we follow the methodology of Costa et al. (53). Briefly, each data point (P_i, δ_i) in the force-indentation curve, where P_i is the loading force and δ_i is the indentation into the material, was substituted into Equation 1 to calculate the corresponding E_i, the Young's modulus at point *i*; the subscript denotes an individual data point along the force-indentation profile.

$$\delta = \left(\frac{9F^2}{16RE^{*2}}\right)^{1/3} \quad \text{(Equation 1)}$$

R is the effective radius of curvature, and E^* is the apparent Young's modulus, defined as $\frac{1}{E^*} = \frac{1-\nu_1^2}{E_1} + \frac{1-\nu_2^2}{E_2}$, where ν_1 and ν_2 are the Poisson's ratio for the material and F is force, and the subscripts denote the two contacting bodies. For all samples tested, the value of δ_i at which the linear-nonlinear regime transition, or δ_L, was between 2 and 3 nN. Thus, we used 2 nN as the nominal value for δ_L and calculated the Young's modulus of 10%–30% of the loading curve for the linearly elastic regime, or E_{low}, and 70%–90% (approximately 6 nN maximum load) for E_{high}. We defined an elasticity metric, $L = E_{low}/E_{high}$, where $L = 1$ is absolute linear elasticity, and values of less than 1 are increasingly nonlinear. Following AFM analysis, samples were fixed in 4% formaldehyde and processed for histological stains (H&E, Masson's trichrome) and immunohistochemistry.

For cell cortical stiffness measurements, cell were plated at 2×10^4 cells/cm^2 and measured within 4–6 hours of plating in full growth medium. Cantilever spring constants were measured prior to sample analysis. Single-force points taken from 3 perinuclear regions of greater than 300 nm in height were averaged to determine a cell's average stiffness. Similarly, regions of PAAm substrate surrounding measured cells were probed. Force indentation measurements were made using an indentation trigger point equal to 1 μm and individually analyzed within the linearly elastic regime as above. For CDM measurements, cells were stained with DiI, and regions within 10 μm of the cell body or projections were measured and compared with regions greater than 10 μm from cells. For cell stiffness measurements, n = 14–22 individual cells were analyzed.

ECM substrate preparation. CDMs were prepared according to Cukierman et al. (21). Briefly, 0.2% gelatin was adsorbed onto coverglass and crosslinked with 1.0% glutaraldehyde. Following quenching with 1 M glycine and PBS washing, NIH-3T3 cells (ATCC) were plated at 5×10^5/ml into a 6-well plate. Cultures were maintained in DMEM supplemented with 10% FBS, 100 μg/ml penicillin/streptomycin, 1 mM sodium pyruvate, and 50 μg/ml ascorbic acid, with media changed every 48 hours. After 8 days, cells were extracted using 0.5% Triton X-100 and 20 mM Na_4OH in PBS, and DNAseI was used to digest remaining nuclear material. CDMs were extensively washed with PBS and stored at 4°C in 100 μg/ml penicillin/streptomycin-supplemented PBS for up to 2 weeks. To solubilize CDMs for subsequent coating of PA gels, CDMs were incubated in a solubilization buffer to denature and solubilize matrix components (5 M guanidine HCl, 10 mM dithiothreitol) for 5 minutes on ice before they were scraped into a 1.5-ml microcentrifuge tube. Solubilization buffer was added up to 500 μl, rotated for 1 hour at 4°C, and centrifuged at 12,000 *g* for 15 minutes. The supernatant was collected and used for sulfo-SANPAH crosslinking to PA gels as described below.

Col1 gels were prepared with acid-solubilized rat tail collagen (Corning). 1 M NaOH was used to neutralize pH at a final concentration of 3.3 mg/ml on 6-well tissue culture–treated plates or a glass-bottom FluoroDish (World Precision Instruments). Approximately 400 μl Col1 solution was used per 6-well dish or equivalent area. Samples were allowed to polymerize for 60 minutes at 37°C before PBS was added or the gels were used as a substrate. For exogenous chemical crosslinking, Col1 gels were incubated in 4% paraformaldehyde for 30 minutes before quenching with 1 M glycine for 30 minutes and extensive washing in PBS. HDFC matrices were made according to Artym et al. (54, 55). Briefly, 8 mg/ml neutralized Col1 solution (high concentration rat tail, Corning) was pipetted on top of prechilled FluoroDishes and spread to create a thin layer using a plastic pipette tip. The thin layer of Col1 was allowed to polymerize at 37°C for 30 minutes. The dishes were centrifuged at 3,500 *g* for 20 minutes, and then matrices were crosslinked with 4% paraformaldehyde/5% sucrose in PBS for 20 minutes. HDFC matrices were washed extensively with PBS before being used for cell culture or AFM experiments.

PA hydrogels with varying bisacrylamide concentrations were fabricated on amino-silanized coverslips, as previously described (15). Briefly, PA gel solutions were produced by combining acrylamide and bisacrylamide (Bio-Rad) to final concentrations of 8% acrylamide and 0.045%, 0.102%, 0.146%, or 0.239% bisacrylamide to obtain gels with final elastic moduli of 1.8, 6.7, 10.6, or 18.7 kPa, respectively. 50 μl of each solution was polymerized by the addition of 1% (v/v) ammonium persulfate (VWR) and 0.1% (v/v) N,N,N′,N′-tetramethylethylenediamine (Bio-Rad). Human plasma FN was purified from blood plasma and covalently attached to the surface using the heterobifunctional crosslinker sulfosuccinimidyl-6-(4′-azido-2′ nitrophenyl-amino)hexanoate (sulfo-SANPAH, Pierce Chemical Co.). Following overnight incubation with FN, gels were washed and stored in PBS.

Cell culture and plasmids. Primary human lung fibroblasts were isolated from healthy subjects or IPF patients as described previously (56). NLFs were obtained from patients undergoing thoracic surgery for nonfibrotic lung diseases. IPF lung fibroblasts were used from patients in whom a pathologic diagnosis of UIP had been made. Under sterile conditions, lung tissue segments were minced to a fine slurry and cultured in T-75 tissue culture flasks. Cells were maintained in DMEM supplemented with 10% FBS, 100 μg/ml penicillin/streptomycin, and 1 mM sodium pyruvate (normal growth medium), and media was replaced every 48 to 72 hours. For fluorescence-activated cell sorting (FACSAria III, BD Biosciences), cells were stained with FITC-labeled anti-human Thy-1 antibody (1:200, 5E10; BD Pharmingen) and sorted into Thy-1–positive and Thy-1–negative subpopulations based on equivalent positive expression of NLFs or negative antibody controls, respectively. Cells were used for experimentation between passages 4 and 9. For Thy-1 knockdown experiments, CCD-19lu NLFs (CCL-210, ATCC) were transduced with lentiviral particles (5× multiplicity of infection plus 5 μg/ml Polybrene [MilliporeSigma]) containing a pool of 19–25 (plus hairpin) nucleotide-encoding target-specific constructs (sc-32837-v, Santa Cruz Biotechnology) or a scrambled sequence control without specificity to any known cellular mRNA (sc-108080, Santa Cruz Biotechnology). After 72 hours, transduced cells were subcultured and selected with 1.0 μg/ml puromycin. Cells were FACS isolated for cells exhibiting high knockdown efficiency, whereas the control shRNA construct had no effect on Thy-1 expression. Four cell lines of unique IPF and control patients were used for the data represented in Figure 2, C–E. In the remainder of experiments, at least two unique cell lines were tested. Independent Thy-1 knockdown and use of the sorted cells for in vitro experiments was performed twice.

Immunostaining of tissues and cells. For immunohistochemistry of tissues, α-SMA (1:200; 1A4, MilliporeSigma) and FN-EDA (1:200; IST-9, Abcam) primary antibodies were used with the ABC horseradish peroxidase or alkaline phosphatase detection kits (Vector Labs) and DAB or vector red substrates, respectively. For immunofluorescence of tissues, 4-μm sections were fixed with 3.7% formaldehyde for 10 minutes, permeabilized with 0.25% Triton X-100 for 15 minutes, and blocked with1% BSA (Amresco) for 1 hour. Lung slides were stained with primary antibody of activated $\alpha_v\beta_3$ integrin (1:200; WOW-1, gift of Sanford Shattil, University of California, San Diego) at 4°C overnight. After the sections were washed with PBS, Alexa Fluor–coupled secondary antibodies (Invitrogen) were used at 1:1,000. Nuclear staining was carried out with DAPI using ProLong Diamond Antifade Mountant medium (P36962, Invitrogen). Fluorescence images were captured on a BZ-X700 microscope (Keyence).

In vitro samples were fixed with 4% formaldehyde for 10 minutes, permeabilized with 0.2% Triton X-100 for 5 minutes, and blocked with 10% normal goat serum. Primary antibodies for MRTF-A (1:200; ab49311, Abcam), vinculin (1:200; V284, MilliporeSigma), $\alpha_v\beta_3$ integrin (1:200; LM609, MilliporeSigma), $\alpha_v\beta_3$ integrin (1 μg/ml; WOW-1), β_1 integrin (1:100; 9EG7, BD), paxillin (1:200; 5H11, MilliporeSigma),

rabbit anti-FAK-pY397 (1:150; Invitrogen), human Thy-1 (1:200; 5E10, BD Pharmingen), and FN (1:300; AB2024, MilliporeSigma), along with Alexa Fluor–labeled secondary antibodies (1:1,000; Invitrogen), were incubated for 1 hour at room temperature or overnight at 4°C. Alexa Fluor–conjugated phalloidin (1:40; Invitrogen) was used to stain F-actin. Samples were stained 1:1,000 with Hoechst 33258 and mounted with ProLong Diamond Antifade Mountant. Images were acquired at a magnification of ×20 (Plan-fluor, 0.5 NA) or ×60 (Plan-apochromat, 1.4 NA) with a Nikon TiE epifluorescence microscope and CoolSNAP HQ2 monochromatic CCD camera (Photometrics) or with a Zeiss LSM700 confocal microscope with variable secondary dichroic and ×20 (0.8 NA) and ×60 (1.4 NA) objectives.

Image quantification. A MATLAB program built in-house was used to quantify micrographs based on the morphometry and intensity of FAs. After background subtraction, an intensity threshold was used to identify and mask structures based on paxillin or active-β_1 integrin signal. Masked pixels were converted to binary sequence, and connected pixels were grouped into bins based on size and converted to μm^2 units. For FAK activity analysis within FAs, paxillin was used as an FA marker in this study, as done previously (57). The paxillin mask was subsequently applied to both adhesion marker channels, and the ratiometric value for FAK-pY397/paxillin intensity was calculated on a per pixel basis. For integrin engagement in FA analysis, FA signal for $\alpha_v\beta_3$ (LM609 mAb) and active β_1 integrin (9EG7 mAb) were segmented, and the ratiometric pixel intensity was calculated. All identified and segmented FAs were averaged for a single cell. Cell area was quantified using a similar intensity-based detection scheme based on phalloidin or DiI staining.

Animal use and bleomycin-induced fibrosis. In a 2 × 5 factorial design, Thy-$1^{-/-}$ (58) and WT mice on C57BL/6 background (18 months old, both male and female) were randomly assigned to 5 groups for this study (n = 8 animals for each group). To generate pulmonary injury and fibrosis, anesthetized (i.p. ketamine, 80 mg/kg; xylazine, 10 mg/kg) mice were orotracheally instilled with bleomycin (4 U/kg BW, Tecoland Corporation) dissolved in sterile saline (100 μl) via MicroSprayer (MS-IA-1C, Penn-Century) or sterile saline for controls. At 14, 28, 42, and 56 days after bleomycin instillation, lung mechanics were performed and lung tissues were processed for histology. Survival percentage was calculated in Thy-$1^{-/-}$ and WT mice throughout 56 days after bleomycin instillation.

Pulmonary mechanics testing and histopathology. Invasive pulmonary mechanics of mice were carried out with a computer-controlled FlexiVent system (SCIREQ) using forced oscillation technique, as previously described (59). Briefly, mice were anesthetized using a mixture of ketamine (80 mg/kg) and xylazine (10 mg/kg) i.p., followed by tracheostomy and tracheal intubation. Then mice were connected to the FlexiVent preprogrammed rodent ventilator at an average breathing frequency of 150 breaths/min. Maneuvers or perturbations of TLC, FlexiVent snapshot, primewave-8, and PVs-P were imposed according to the manufacturer's protocols. All maneuvers or perturbations were performed in triplicate. The more relevant specific parameters for restrictive respiratory diseases (elastance [E] and P-V curve with a determination coefficient of ≥0.95) were used to analyze the changes in lung mechanics. After mechanical testing, lungs were fixed (10% formalin at a constant pressure of 20 cm H_2O) and paraffin embedded.

Statistics. Statistical tests were performed using Prism (version 7.0b, GraphPad). One-way ANOVA and Newman-Keuls for multiple comparisons or Kruskal-Wallis nonparametric test with Dunn's for multiple comparisons were used to calculate statistical significance. P values of less than 0.05 were considered significant, and P values are indicated in the appropriate figure legends.

Study approval. Human deidentified IPF lung samples were obtained from explants of patients with IPF undergoing lung transplantation at the University of Michigan. Written informed consent was obtained from all subjects in accordance with the University of Michigan Institutional Review Board. The University of Michigan Institutional Review Board deemed these approaches exempt from oversight, as all subjects were considered deceased. The mice were housed at the University of California, San Diego School of Medicine (La Jolla, California, USA) animal facility in accordance with guidelines from the Association for the Assessment and Accreditation for Laboratory Animal Care International. The University of California, San Diego School of Medicine Institutional Animal Care and Use Committee of approved all experimental protocols.

Author contributions

VFF and THB conceptualized and initiated the project. VFF designed and conducted all AFM and in vitro experiments. C. Tran, WX, and TS assisted with AFM experiments and data analysis. SSW, C. Tan, and JH conducted in vivo experiments. ESW provided human samples. VFF and THB wrote the manuscript with edits from ESW and JSH.

Acknowledgments

Funding was provided by the National Institutes of Health through grants R01HL127283 and R01HL132585 to THB and R01HL111169 to JSH; and the National Science Foundation through grant NSF 1538161 to TS; and a National Science Foundation Graduate Research Fellowship to VFF.

Address correspondence to: Thomas H. Barker, Box 800759, 415 Lane Road (MR5 Building), University of Virginia, Charlottesville, Virginia 22908, USA. Phone: 434.297.7990; Email: thomas.barker@virginia.edu (T.H. Barker). Or to: Vincent F. Fiore, 1230 York Ave., New York, New York 10065, USA. Phone: 404.327.7482; Email: vfiore@rockefeller.edu (V.F. Fiore).

VFF's present address is: The Rockefeller University, New York, New York, USA.

JSH's present address is: Department of Pediatrics, Division of Pulmonology, University of North Carolina at Chapel Hill, Chapel Hill, North Carolina, USA.

1. Butcher DT, Alliston T, Weaver VM. A tense situation: forcing tumour progression. *Nat Rev Cancer*. 2009;9(2):108–122.
2. Tomasek JJ, Gabbiani G, Hinz B, Chaponnier C, Brown RA. Myofibroblasts and mechano-regulation of connective tissue remodelling. *Nat Rev Mol Cell Biol*. 2002;3(5):349–363.
3. Yamauchi M, Barker TH, Gibbons DL, Kurie JM. The fibrotic tumor stroma. *J Clin Invest*. 2018;128(1):16–25.
4. Zhou Y, et al. Inhibition of mechanosensitive signaling in myofibroblasts ameliorates experimental pulmonary fibrosis. *J Clin Invest*. 2013;123(3):1096–1108.
5. Blackwell TS, et al. Future directions in idiopathic pulmonary fibrosis research. An NHLBI workshop report. *Am J Respir Crit Care Med*. 2014;189(2):214–222.
6. Parker MW, et al. Fibrotic extracellular matrix activates a profibrotic positive feedback loop. *J Clin Invest*. 2014;124(4):1622–1635.
7. Cool CD, Groshong SD, Rai PR, Henson PM, Stewart JS, Brown KK. Fibroblast foci are not discrete sites of lung injury or repair: the fibroblast reticulum. *Am J Respir Crit Care Med*. 2006;174(6):654–658.
8. Yeung T, et al. Effects of substrate stiffness on cell morphology, cytoskeletal structure, and adhesion. *Cell Motil Cytoskeleton*. 2005;60(1):24–34.
9. Wipff PJ, Rifkin DB, Meister JJ, Hinz B. Myofibroblast contraction activates latent TGF-beta1 from the extracellular matrix. *J Cell Biol*. 2007;179(6):1311–1323.
10. Liu F, et al. Feedback amplification of fibrosis through matrix stiffening and COX-2 suppression. *J Cell Biol*. 2010;190(4):693–706.
11. Chang HY, et al. Diversity, topographic differentiation, and positional memory in human fibroblasts. *Proc Natl Acad Sci USA*. 2002;99(20):12877–12882.
12. Sorrell JM, Caplan AI. Fibroblast heterogeneity: more than skin deep. *J Cell Sci*. 2004;117(Pt 5):667–675.
13. Visscher DW, Myers JL. Histologic spectrum of idiopathic interstitial pneumonias. *Proc Am Thorac Soc*. 2006;3(4):322–329.
14. Booth AJ, et al. Acellular normal and fibrotic human lung matrices as a culture system for in vitro investigation. *Am J Respir Crit Care Med*. 2012;186(9):866–876.
15. Brown AC, Fiore VF, Sulchek TA, Barker TH. Physical and chemical microenvironmental cues orthogonally control the degree and duration of fibrosis-associated epithelial-to-mesenchymal transitions. *J Pathol*. 2013;229(1):25–35.
16. Broedersz CP, MacKintosh FC. Modeling semiflexible polymer networks. *Rev Mod Phys*. 2014;86:995.
17. Nho RS, Hergert P, Kahm J, Jessurun J, Henke C. Pathological alteration of FoxO3a activity promotes idiopathic pulmonary fibrosis fibroblast proliferation on type i collagen matrix. *Am J Pathol*. 2011;179(5):2420–2430.
18. Xia H, et al. Pathological integrin signaling enhances proliferation of primary lung fibroblasts from patients with idiopathic pulmonary fibrosis. *J Exp Med*. 2008;205(7):1659–1672.
19. Olson EN, Nordheim A. Linking actin dynamics and gene transcription to drive cellular motile functions. *Nat Rev Mol Cell Biol*. 2010;11(5):353–365.
20. Huang X, et al. Matrix stiffness-induced myofibroblast differentiation is mediated by intrinsic mechanotransduction. *Am J Respir Cell Mol Biol*. 2012;47(3):340–348.
21. Cukierman E, Pankov R, Stevens DR, Yamada KM. Taking cell-matrix adhesions to the third dimension. *Science*. 2001;294(5547):1708–1712.
22. Fiore VF, Strane PW, Bryksin AV, White ES, Hagood JS, Barker TH. Conformational coupling of integrin and Thy-1 regulates Fyn priming and fibroblast mechanotransduction. *J Cell Biol*. 2015;211(1):173–190.
23. Pampori N, et al. Mechanisms and consequences of affinity modulation of integrin alpha(V)beta(3) detected with a novel patch-engineered monovalent ligand. *J Biol Chem*. 1999;274(31):21609–21616.
24. Georges PC, et al. Increased stiffness of the rat liver precedes matrix deposition: implications for fibrosis. *Am J Physiol Gastrointest Liver Physiol*. 2007;293(6):G1147–G1154.
25. King TE, Pardo A, Selman M. Idiopathic pulmonary fibrosis. *Lancet*. 2011;378(9807):1949–1961.
26. King TE, et al. Idiopathic pulmonary fibrosis: relationship between histopathologic features and mortality. *Am J Respir Crit Care Med*. 2001;164(6):1025–1032.
27. Ley B, Collard HR, King TE. Clinical course and prediction of survival in idiopathic pulmonary fibrosis. *Am J Respir Crit Care Med*. 2011;183(4):431–440.
28. Nicholson AG, Fulford LG, Colby TV, du Bois RM, Hansell DM, Wells AU. The relationship between individual histologic features and disease progression in idiopathic pulmonary fibrosis. *Am J Respir Crit Care Med*. 2002;166(2):173–177.

29. Bates JH, Maksym GN, Navajas D, Suki B. Lung tissue rheology and 1/f noise. *Ann Biomed Eng*. 1994;22(6):674–681.
30. Yuan H, Ingenito EP, Suki B. Dynamic properties of lung parenchyma: mechanical contributions of fiber network and interstitial cells. *J Appl Physiol*. 1997;83(5):1420–1431.
31. Ebihara T, Venkatesan N, Tanaka R, Ludwig MS. Changes in extracellular matrix and tissue viscoelasticity in bleomycin-induced lung fibrosis. Temporal aspects. *Am J Respir Crit Care Med*. 2000;162(4 Pt 1):1569–1576.
32. Suki B, Ito S, Stamenovic D, Lutchen KR, Ingenito EP. Biomechanics of the lung parenchyma: critical roles of collagen and mechanical forces. *J Appl Physiol*. 2005;98(5):1892–1899.
33. Roca-Cusachs P, del Rio A, Puklin-Faucher E, Gauthier NC, Biais N, Sheetz MP. Integrin-dependent force transmission to the extracellular matrix by α-actinin triggers adhesion maturation. *Proc Natl Acad Sci USA*. 2013;110(15):E1361–E1370.
34. Schiller HB, et al. β1- and αv-class integrins cooperate to regulate myosin II during rigidity sensing of fibronectin-based microenvironments. *Nat Cell Biol*. 2013;15(6):625–636.
35. Balcioglu HE, van Hoorn H, Donato DM, Schmidt T, Danen EH. The integrin expression profile modulates orientation and dynamics of force transmission at cell-matrix adhesions. *J Cell Sci*. 2015;128(7):1316–1326.
36. Elosegui-Artola A, et al. Rigidity sensing and adaptation through regulation of integrin types. *Nat Mater*. 2014;13(6):631–637.
37. Elosegui-Artola A, et al. Mechanical regulation of a molecular clutch defines force transmission and transduction in response to matrix rigidity. *Nat Cell Biol*. 2016;18(5):540–548.
38. Chen Y, Lee H, Tong H, Schwartz M, Zhu C. Force regulated conformational change of integrin αVβ3. *Matrix Biol*. 2017;60-61:70–85.
39. Henderson NC, et al. Targeting of αv integrin identifies a core molecular pathway that regulates fibrosis in several organs. *Nat Med*. 2013;19(12):1617–1624.
40. Zhou WQ, Wang P, Shao QP, Wang J. Lipopolysaccharide promotes pulmonary fibrosis in acute respiratory distress syndrome (ARDS) via lincRNA-p21 induced inhibition of Thy-1 expression. *Mol Cell Biochem*. 2016;419(1-2):19–28.
41. Sueblinvong V, et al. Predisposition for disrepair in the aged lung. *Am J Med Sci*. 2012;344(1):41–51.
42. Barker TH, et al. Thy-1 regulates fibroblast focal adhesions, cytoskeletal organization and migration through modulation of p190 RhoGAP and Rho GTPase activity. *Exp Cell Res*. 2004;295(2):488–496.
43. Barker TH, et al. Thrombospondin-1-induced focal adhesion disassembly in fibroblasts requires Thy-1 surface expression, lipid raft integrity, and Src activation. *J Biol Chem*. 2004;279(22):23510–23516.
44. Hagood JS, Lasky JA, Nesbitt JE, Segarini P. Differential expression, surface binding, and response to connective tissue growth factor in lung fibroblast subpopulations. *Chest*. 2001;120(1 Suppl):64S–66S.
45. Hagood JS, Mangalwadi A, Guo B, MacEwen MW, Salazar L, Fuller GM. Concordant and discordant interleukin-1-mediated signaling in lung fibroblast thy-1 subpopulations. *Am J Respir Cell Mol Biol*. 2002;26(6):702–708.
46. Hagood JS, et al. Differential expression of platelet-derived growth factor-alpha receptor by Thy-1(-) and Thy-1(+) lung fibroblasts. *Am J Physiol*. 1999;277(1 Pt 1):L218–L224.
47. Liu X, et al. Thy-1 interaction with Fas in lipid rafts regulates fibroblast apoptosis and lung injury resolution. *Lab Invest*. 2017;97(3):256–267.
48. Zhou Y, Hagood JS, Murphy-Ullrich JE. Thy-1 expression regulates the ability of rat lung fibroblasts to activate transforming growth factor-beta in response to fibrogenic stimuli. *Am J Pathol*. 165(2):659–669.
49. Zhou Y, Hagood JS, Lu B, Merryman WD, Murphy-Ullrich JE. Thy-1-integrin alphav beta5 interactions inhibit lung fibroblast contraction-induced latent transforming growth factor-beta1 activation and myofibroblast differentiation. *J Biol Chem*. 2010;285(29):22382–22393.
50. Hagood JS, et al. Loss of fibroblast Thy-1 expression correlates with lung fibrogenesis. *Am J Pathol*. 2005;167(2):365–379.
51. Sanders YY, et al. Thy-1 promoter hypermethylation: a novel epigenetic pathogenic mechanism in pulmonary fibrosis. *Am J Respir Cell Mol Biol*. 2008;39(5):610–618.
52. Butler JP, Nakamura M, Sasaki H, Sasaki T, Takishima T. Poissons' ratio of lung parenchyma and parenchymal interaction with bronchi. *Jpn J Physiol*. 1986;36(1):91–106.
53. Costa KD, Sim AJ, Yin FC. Non-Hertzian approach to analyzing mechanical properties of endothelial cells probed by atomic force microscopy. *J Biomech Eng*. 2006;128(2):176–184.
54. Artym VV, et al. Dense fibrillar collagen is a potent inducer of invadopodia via a specific signaling network. *J Cell Biol*. 2015;208(3):331–350.
55. Artym VV. Preparation of high-density fibrillar collagen matrices that mimic desmoplastic tumor stroma. *Curr Protoc Cell Biol*. 2016;70:10.19.1–10.19.11.
56. White ES, et al. Integrin alpha4beta1 regulates migration across basement membranes by lung fibroblasts: a role for phosphatase and tensin homologue deleted on chromosome 10. *Am J Respir Crit Care Med*. 2003;168(4):436–442.
57. Fiore VF, Ju L, Chen Y, Zhu C, Barker TH. Dynamic catch of a Thy-1-α5β1+syndecan-4 trimolecular complex. *Nat Commun*. 2014;5:4886.
58. Barlow JZ, Kelley KA, Bozdagi O, Huntley GW. Testing the role of the cell-surface molecule Thy-1 in regeneration and plasticity of connectivity in the CNS. *Neuroscience*. 2002;111(4):837–852.
59. Manali ED, et al. Static and dynamic mechanics of the murine lung after intratracheal bleomycin. *BMC Pulm Med*. 2011;11:33.